Supplement of Earth Syst. Dynam., 17, 829–841, 2026
https://doi.org/10.5194/esd-17-829-2026-supplement

Earth System Dynamics
Open Access
EGU

Supplement of

Emergent constraints on climate sensitivity and recent record-breaking warm years

Patric J. L. Boardman et al.

Correspondence to: Patric J. L. Boardman (pb662@exeter.ac.uk)

S1 Derivations

S1.1 The Two-Layer Energy Balance Model

The one- and two-layer (referred to as one- and two-box) energy balance climate models (Caldeira and Myhrvold, 2013; Geoffroy et al., 2013; Gregory, 2000; Winton et al., 2010) provide the theoretical framework predicting a relationship between the change in GMST and climate sensitivity (Jiménez-de-la-Cuesta and Mauritsen, 2019; Nijsse et al., 2020; Tokarska et al., 2020). The two-layer model consists of two differential equations; with each one describing the temperature evolution over time in each layer. Physically, the top layer corresponds to the composite of both the atmosphere and the upper ocean, whereas the bottom layer corresponds to the deep ocean. The model is given by

$$\begin{aligned} C\frac{dT}{dt} &= Q - \lambda T - \varepsilon\gamma(T - T_0), \\ C_0\frac{dT_0}{dt} &= \gamma(T - T_0), \end{aligned} \tag{S1}$$

where each equation represents the equilibrium energy balance in the top and bottom layers respectively. Here, T is the top layer temperature anomaly, T_0 the deep-ocean temperature anomaly, Q is the radiative forcing, λ is the feedback parameter, ε is the ocean heat uptake efficacy, and γ is the ocean heat uptake. The parameters C and C_0 are the heat capacities of the upper and deep oceans, respectively. In the case of there being a radiative imbalance, we can define N as the total rate of change of energy flux of the system,

$$N = CdT/dt + C_0 dT_0/dt \tag{S2}$$

which physically represents the top-of-the-atmosphere radiative flux which has to leave in order to maintain energetic conservation. To develop a diagnostic model, we follow the assumptions outlined in Williamson et al., 2018 and Jiménez-de-la-Cuesta and Mauritsen, 2019, namely that the deep-ocean temperature is constant ($T_0 = 0$), and that the upper ocean is in equilibrium ($dT/dt = 0$). These assumptions are valid for timescales which are longer than a decade, but shorter than a century. The diagnostic equations are therefore

$$\begin{aligned} 0 &= Q - (\lambda - \varepsilon\gamma)T, \\ N &= \gamma T. \end{aligned} \tag{S3}$$

From these equations, we are able to diagnose both climate sensitivity metrics.

S1.1.1 TCR

In the case of a 1 % rise in CO_2, the cumulative concentration of CO_2 will increase exponentially over time. However, due to the logarithmic relationship between Q and changes in the concentration of CO_2 (Huang and Bani Shahabadi, 2014), the resulting temporal relationship of Q is linear. Therefore, a given n-fold increase in CO_2 will always occur at a set time after $t = 0$. Calculation of the TCR uses a doubling of CO_2 as a reference, therefore, the time taken for a doubling of CO_2 to happen, $t_{2\times}$, is given by

$$t_{2\times} = \frac{\ln(2)}{\ln(1.01)} = 69.67\text{yr}. \tag{S4}$$

at which time the forcing is exactly $Q(t_{2\times}) \equiv Q_{2\times}$. By defining the TCR as the change in temperature when $Q(t) = Q_{2\times}$, we obtain

$$\text{TCR} = \frac{Q_{2\times}}{\lambda - \varepsilon\gamma}. \tag{S5}$$

We also observe that the relationship between any change of Q and the resulting change in T is linear. $\frac{\Delta T}{\Delta Q} = (\lambda - \varepsilon\gamma)^{-1}$ which allows us to write the TCR as

$$\text{TCR} = \frac{Q_{2\times}}{\Delta Q}\Delta T = s\Delta T, \tag{S6}$$

where $s \equiv Q_{2\times}/\Delta Q$ is the emergent proportionality constant, referred to as the forcing parameter. For the purposes of fitting, we allow for an intercept of the TCR axis to account for model offsetting, so the equation becomes

$$\text{TCR} = s\Delta T + \eta, \tag{S7}$$

where η is an arbitrary constant.

S1.1.2 ECS

An abrupt n-fold increase in CO_2 results in the radiative forcing resembling a Heaviside step-function, with the instantaneous increase in forcing to a value Q_0 occurring at $t = 0$. ECS is normally quoted in terms of a doubling of CO_2, where $Q_0 = Q_{2\times}$. Since ECS characterises a long term temperature change, the ocean is assumed to be in equilibrium. Therefore

$$\text{ECS} = \frac{Q_{2\times}}{\lambda} \tag{S8}$$

Using this to elimatatie λ from the diagnostic equations, we obtain

$$\text{ECS} = \frac{Q_{2\times}\Delta T}{\Delta Q + \varepsilon\gamma\Delta T} = \frac{\Delta T}{s^{-1} - e\Delta T}. \tag{S9}$$

where $e \equiv \varepsilon\gamma/Q_{2\times}$ is the ocean uptake parameter. Equation (S9) has an asymptote at the value $\Delta T = 1/se$, and then turns negative for $\Delta T > 1/se$. As negative ECS values are unphysical, the domain is restricted to ECS $< 1/se$. By combining both equations, we can express the ECS in terms of the TCR:

$$\text{ECS} = \frac{\text{TCR}}{1 - e\text{TCR}} \tag{S10}$$

S1.2 Ordinary Least-Squares Linear Regression

The basis for Ordinary Least-Squares (OLS) fitting is well established (**wolframLeastSquares**), and the emergent relationships both have the following linear form:

$$y_n = a + bx_n \tag{S11}$$

which we model using

$$f(x) = a + bx \tag{S12}$$

Finding the coefficients a and b involves minimising the least-squares sum

$$s^2 = \frac{1}{N-2}\sum_{n=1}^{N}(y_n - f(x_n))^2 \tag{S13}$$

where N is the number of data points, and we divide by a factor of $N-2$ to account for the number of degrees of freedom. For our analysis, we are interested in the best fit gradient $\bar{b}$ and standard error σ_b of this fit. These are given by

$$\bar{b} = \frac{\sigma_{xy}^2}{\sigma_x^2}, \tag{S14}$$

$$\sigma_b = \frac{s}{\sigma_x\sqrt{N}}. \tag{S15}$$

Here, $\sigma_x^2 = \text{var}(x) = \sum_{n=1}^{N}(x_n - \bar{x})^2/N$ is the variance of x_n and $\sigma_{xy} = \text{cov}(x, y) = \sum_{n=1}^{N}(x_n - \bar{x})(y_n - \bar{y})/N$ is the covariance of x_n and y_n, with means of $\bar{x}$ and $\bar{y}$ respectively. We assume that best fit gradient follows a normal distribution, with mean $\bar{b}$ and variance σ_b^2

$$P(b) = \frac{1}{\sqrt{2\pi\sigma_b^2}}\exp\left(-\frac{(b-\bar{b})^2}{2\sigma_b^2}\right) \tag{S16}$$

Using the both the variance in the datasets as well as the uncertainty in the best-fit parameters, we can calculate the resulting uncertainty of our model $f(x)$, σ_f:

$$\sigma_f(x) = s\sqrt{1 + \frac{1}{N} + \frac{(x - \bar{x})}{N\sigma_x^2}}, \tag{S17}$$

which represents the uncertainty in a prediction using our model $f(x)$ for a known value of x

$$P(y|x) = \frac{1}{\sqrt{2\pi\sigma_f^2(x)}} \exp\left(-\frac{(y - f(x))^2}{2\sigma_f^2(x)}\right). \tag{S18}$$

Finally, to generate the full PDF of our constrained variable y, we must make use of a known value of our observable. This can be characterised in terms of a PDF for x, $P(x)$. Assuming that this also follows a normal distribution centred on x_{obs} with a known error, $\sigma_{x_{obs}}$, then $P(y)$, can be calculating by integrating the product of the two the probabilities across the entire domain of x:

$$P(y) = \int_{\infty}^{\infty} P(y|x)P(x)dx \tag{S19}$$

S2 Robustness of TCR

S2.1 TCR Dependence on Start Year, Window size and End Year

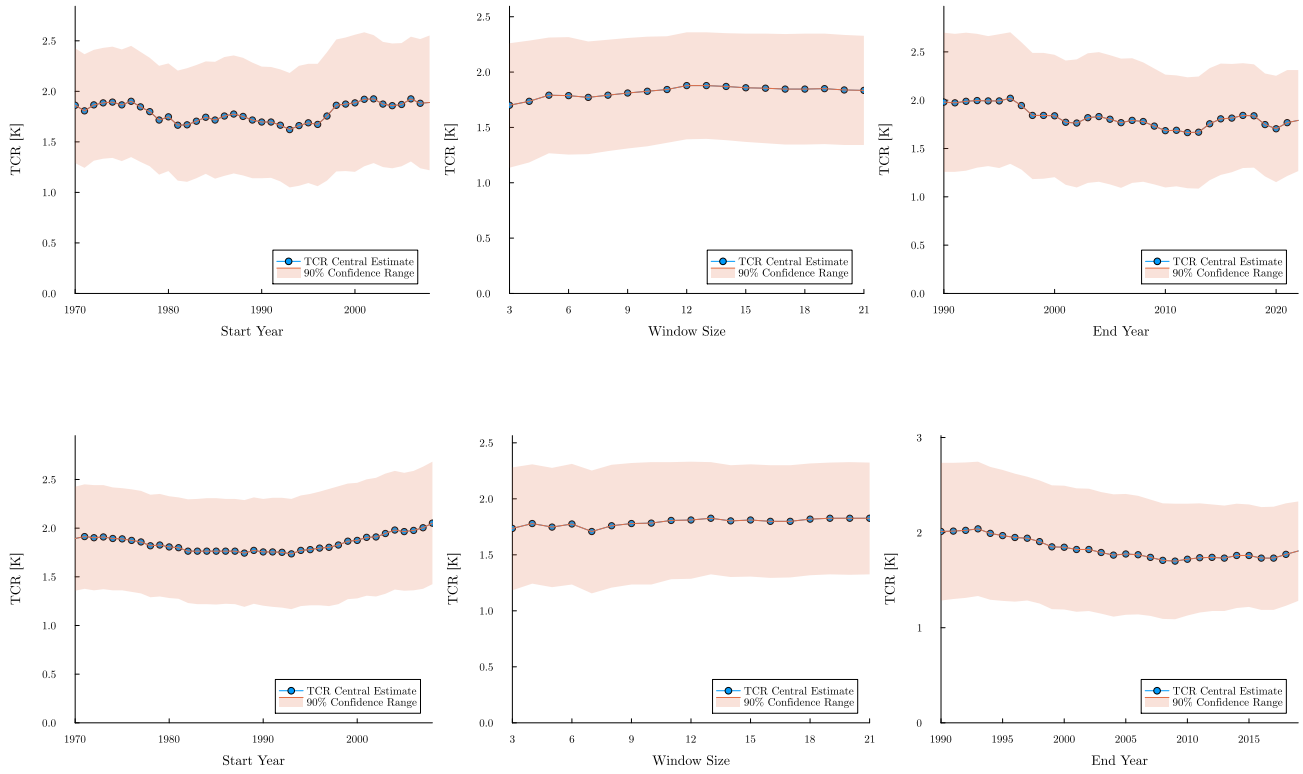

Figure S1: TCR robustness checks based on sensitivity to various parameter choices. Unless stated otherwise, the central start year is 1980 and all years up to 2024 are used. Except for the two central plots, where the smoothing window is varied, the top three plots use a default 5-year smoothing window, while the bottom three use an 11-year window. **Left:** Varying central start year from 1970 until 2008. **Middle:** Varying smoothing window from 3 to 21 years. **Right:** Varying central end year from 1990 to the latest year possible for the given smoothing window (i.e., 2022 for the 5-year window and 2019 for the 11-year window).

S2.2 TCR Dependence on SSP Run

S2.2 shows the dependence of the final TCR result on the SSP scenario.

SSP Scenario	**Number of Models**	**TCR 1975–2019** [K]	**TCR 1975–2024** [K]
SSP1-2.6	28	1.74 (1.23–2.24)	1.75 (1.28–2.22)
SSP2-4.5	31	1.76 (1.21–2.30)	1.81 (1.28–2.33)
SSP3-7.0	27	1.76 (1.21–2.31)	1.83 (1.31–2.33)
SSP5-8.5	30	1.75 (1.22–2.27)	1.76 (1.26–2.27)

Table S1: TCR estimates by SSP scenario, showing median and 5–95% range for each period.

S2.3 TCR Dependence on Ensemble Member Combinations

Figure S2 shows the TCR result for a sample of 10000 of the 2.92×10^{11} combinations of available ensemble member runs.

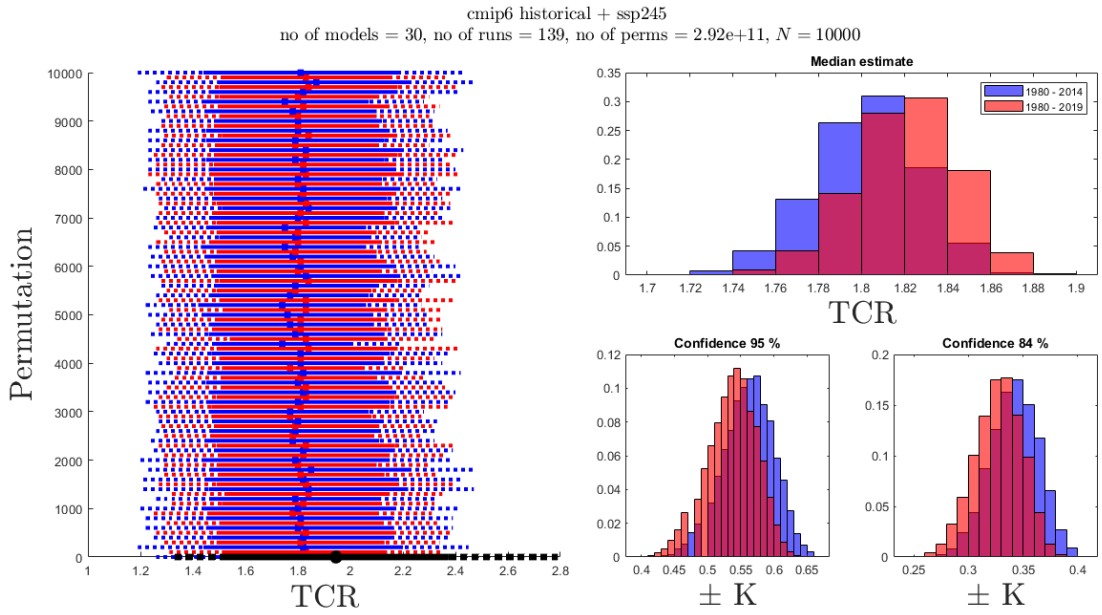

Figure S2: TCR results using a random selection of model initialisation conditions (rxixpxfx), where x is any value in the subset of simulation runs performed by the model centre. **Left:** The TCR prediction distribution across a sample of 10^4 model run selections. For each permutation, filled regions show the 84% confidence range, and dashed regions show the 95% confidence range. **Upper Right:**. Histogram of the central TCR prediction across simulation permutation, with both the periods 1975-2019 (shown in blue) and 1975 - 2024 (shown in red). **Lower Right:** Histograms of both 84% and 95% uncertainty ranges across simulation permutations, with both the periods 1975-2019 (shown in blue) and 1975 - 2024 (shown in red) for each plot.

S3 Internal Variability Analysis of Control and Historical Runs

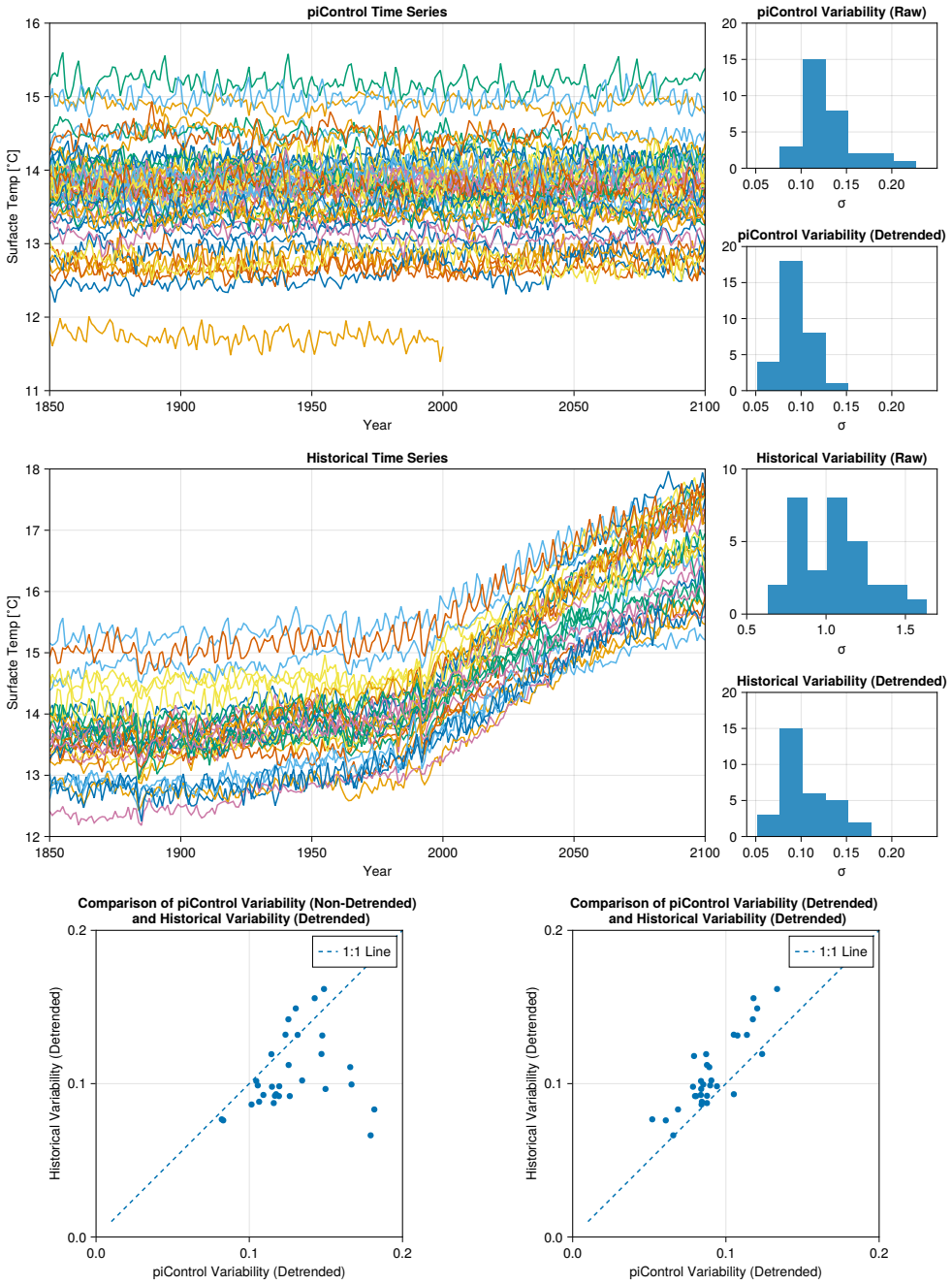

Figure S3: Internal Variability analysis of all control and historical time series runs. **Top left**: GMSAT time series runs of all control runs across the available models. **Middle Left**: GMSAT time series runs of all historical runs across the available models. **Right Column**: Histogram plots showing the distribution of standard deviation (σ) of all GMSAT values in the time series for each model, carried out for raw and detrended versions of both control and historical runs. Since there is a forcing signal, we note that the histogram for the internal variability of the raw version of the historical runs is substantially larger than the other three, though we include it for completeness. **Bottom Left**: Scatter plot comparing the non-detrended control run with the detrended historical run. **Bottom Right**: Scatter plot comparing control and historical runs where both have been detrended.

The panels in Figure S3 show analysis of the internal variability of all available control and historical simulations across the ESMs. We quantify the internal variability by computing the standard deviation of all points in each time series, both relative to a running mean and globally. The former is referred to as 'detrended' variability, as it quantifies the standard deviation of residuals relative to a smoothed running mean, rather than the standard deviation computed from the raw time series. We keep to the same window size of $N = 11$ years used throughout the study. We note the model with the maximum discrepancy between the historical and control variability is the CNRM-CM6-1-HR model, differing by a factor of 2.701 when comparing the un-detrended control run with the detrended historical run.

References

Caldeira, K., & Myhrvold, N. P. (2013). Projections of the pace of warming following an abrupt increase in atmospheric carbon dioxide concentration. *Environmental Research Letters*, *8*(3), 034039. https://doi.org/10.1088/1748-9326/8/3/034039

Geoffroy, O., Saint-Martin, D., Olivié, D. J., Voldoire, A., Bellon, G., & Tytéca, S. (2013). Transient climate response in a two-layer energy-balance model. part i: Analytical solution and parameter calibration using cmip5 aogcm experiments. *Journal of climate*, *26*(6), 1841–1857. https://doi.org/10.1175/JCLI-D-12-00195.1

Gregory, J. M. (2000). Vertical heat transports in the ocean and their effect on time-dependent climate change. *Climate Dynamics*, *16*(7), 501–515. https://doi.org/10.1007/s003820000059

Huang, Y., & Bani Shahabadi, M. (2014). Why logarithmic? a note on the dependence of radiative forcing on gas concentration. *Journal of Geophysical Research: Atmospheres*, *119*(24), 13–683. https://doi.org/10.1002/2014JD022466

Jiménez-de-la-Cuesta, D., & Mauritsen, T. (2019). Emergent constraints on earth's transient and equilibrium response to doubled co2 from post-1970s global warming. *Nature Geoscience*, *12*(11), 902–905. https://doi.org/10.1038/s41561-019-0463-y

Nijsse, F. J., Cox, P. M., Williamson, M. S., & Huntingford, C. M. (2020). Emergent constraints on transient climate response (tcr) and equilibrium climate sensitivity (ecs) from historical warming in cmip5 and cmip6 models. *Earth System Dynamics*, *11*(3), 737–750. https://doi.org/10.5194/esd-11-737-2020

Tokarska, K. B., Stolpe, M. B., Sippel, S., Fischer, E. M., Smith, C. J., Lehner, F., & Knutti, R. (2020). Past warming trend constrains future warming in cmip6 models. *Science advances*, *6*(12), eaaz9549. https://doi.org/10.1126/sciadv.aaz9549

Williamson, M. S., Cox, P. M., & Nijsse, F. J. (2018). Theoretical foundations of emergent constraints: Relationships between climate sensitivity and global temperature variability in conceptual models. *Dynamics and Statistics of the Climate System*, *3*(1), dzy006. https://doi.org/10.1093/climsys/dzy006

Winton, M., Takahashi, K., & Held, I. M. (2010). Importance of ocean heat uptake efficacy to transient climate change. *Journal of Climate*, *23*(9), 2333–2344. https://doi.org/10.1175/2009JCLI3139.1